Lifetimes of Overshooting Convective Events using High-Frequency Gridded Radar Composites

Daniel Jellis,[a] Kenneth P. Bowman,[a] Anita D. Rapp,[a]

[a] *Texas A&M University*

Corresponding author: Daniel Jellis, drjellis@tamu.edu

ABSTRACT: Deep convection that penetrates the tropopause, referred to here as overshooting convection, is capable of lifting tropospheric air well into the stratosphere. In addition to water, these overshoots also transport various chemical species, affecting chemistry and radiation in the stratosphere. It is not currently known, however, how much transport is a result of this mechanism. To better understand overshooting convection, this study aims to characterize the durations of overshooting events. To achieve this, radar data from the Next Generation Weather Radar (NEXRAD) network is composited onto a three-dimensional grid at 5-minute intervals. Overshoots are identified by comparing echo-top heights with tropopause estimates derived from ERA5 reanalysis data. These overshoots are linked in space from one analysis time to the next to form tracks. This process is performed for twelve 4-day sample windows in the months May-August of 2017-2019. Track characteristics such as duration, overshoot area, tropopause-relative altitude, and column-maximum reflectivity are investigated. Positive correlations are found between track duration and other track characteristics. Integrated track volume is found as a product of the overshoot area, depth, and duration, and provides a measure of the potential stratospheric impact of each track. Short-lived tracks are observed to contribute the most total integrated volume when considering track duration, while tracks that overshoot by 2-3 km show the largest contribution when considering overshoot depth. A diurnal cycle is observed, with peak track initiation around 16-17 local time. Track-mean duration peaks a few hours earlier, while track-mean area and tropopause-relative height peak a few hours later.

1. Introduction

The transport of air from the troposphere to the stratosphere is dominated by the Brewer-Dobson circulation, characterized by diabatic upwelling in the tropics and downwelling near the poles (Brewer 1949; Dobson 1956). This global circulation is the primary mechanism for transport of species with long lifetimes in the troposphere, such as CFCs or CO_2, into the stratosphere. The vertical velocity of this tropical upwelling is very slow, around 0.2 mm/s (Flury et al. 2013; Minschwaner and Jiang 2016), meaning that shorter-lived species tend to be removed by oxidation and/or wet-deposition processes before reaching the stratosphere. At mid-latitudes, stratosphere-troposphere exchange (STE) occurs mostly as the result of tropopause folding. Through this process stratospheric air intrudes to lower altitudes and is irreversibly mixed into the troposphere. It has been shown, however, that deep convection is capable of penetrating the tropopause in the mid-latitudes, and that it is a frequent enough occurance to represent a significant stratospheric transport mechanism (Solomon et al. 2016; Cooney et al. 2018; Homeyer and Bowman 2021). O'Neill et al. (2021) find that the overshooting tops of these storms are capable of deflecting the stratospheric flow, enabling a hydraulic jump downstream. This is one possible mixing mechanism through which deep convection may inject water vapor (along with many short- and long-lived chemical species) into the stratosphere. It is vital to understand the magnitude of this transport and its dependence on the size, depth, duration and geographical distribution of overshooting events, as the various constituents can have an impact on the chemistry and radiative equilibrium of the stratosphere (Aschmann et al. 2011; Tang et al. 2011; Sargent et al. 2014; Randel et al. 2015; Yu et al. 2020; Zou et al. 2021). Cooney et al. (2018) analyzed the geographical distribution of overshooting convection in the U.S., along with its diurnal and annual cycles; here we focus on the lifetimes of overshooting events.

Deep convection can occur anywhere there is sufficient instability, but is more likely to penetrate into the stratosphere (hereafter overshooting) in areas where the tropopause is lower (Cooney et al. 2018). Ideal conditions for overshooting are present across North America in the late spring and summer months, with the Great Plains region in the central US being a major hotspot (Liu and Liu 2016; Solomon et al. 2016). The summer anticyclone that regularly forms over North America may act to contain the material injected by deep convection in this region, which can prolong the period before the substances are diluted. The potential to sample both fresh and aged outflow from overshooting events makes this region an attractive target for aircraft campaigns such as the Dynamics and Chemistry of the Summer Stratosphere (DCOTSS) mission.

An important part of the DCOTSS mission, and any study investigating deep convection, is the remote detection of overshooting events. Multiple techniques exist for the identification of overshooting cloud tops (OTs). One option is the use of infrared and visible satellite imagery (Bedka 2011; Mikuš and Strelec Mahović 2013; Bedka et al. 2018b), such as from NOAA's Geostationary Operational Environmental Satellites (GOES). Material injection due to an OT often results in an Above Anvil Cirrus Plume (AACP) several kilometers above the anvil (Bedka et al. 2018a). The AACP may be warmer or colder than the surrounding anvil, making automated detection using IR imagery difficult. Visible imagery may be used to detect shadows cast on the anvil by the AACP, however this method depends on the solar zenith angle and is naturally only feasible during the daytime. Another option for the detection of OTs is weather radar. By comparing radar echo heights with a tropopause height analysis, it is possible to identify storms that overshoot the tropopause (Solomon et al. 2016; Cooney et al. 2018). This technique avoids the difficulties presented by satellite detection, but has limitations arising from radar coverage, spacing between radar sweep angles, and uncertainty in the derived tropopause altitude.

While our knowledge of when and where overshooting convection occurs is improving, there is still much that is not well understood. Some topics of interest include how much material is transported to the stratosphere, how long injected material remains, the impact of overshooting on stratospheric chemistry, what environmental conditions are favorable for overshooting, and how climate change will affect the frequency of overshoots in the future. As a step toward understanding the processes that transport material from the troposphere to the stratosphere through deep convection, this research aims to characterize the lifetimes of overshooting events using observations. Using methods similar to those employed in Cooney et al. (2018), overshooting storm analyses are generated from the Next Generation Weather Radar (NEXRAD) network. However, while Cooney et al. (2018) provides a very useful hourly climatology of overshooting events, there is no information available on the durations of these events due to the relatively low analysis frequency. To this end, radar analyses are conducted across the continental United States at 5-minute intervals in this study, which is approximately the time required for a NEXRAD radar to complete a volume scan when observing convection. Identified overshooting regions are then linked between timesteps based on proximity in order to form overshoot tracks. A total of twelve 5-day analysis periods are used, covering the middle of each summer month (May - August) for the years 2017-2019. This provides a multi-year sample of overshooting tracks across the warm-season months, which allows estimation of the statistics of overshooting-event durations. This information is vital for any estimates of mass transport as a result of overshooting storms.

2. Data

a. NEXRAD

NEXRAD comprises 160 WSR-88D high resolution S-band Doppler radars worldwide, 143 of which provide nearly complete coverage over the contiguous United States, as shown in Figure 1 (Crum and Alberty 1993). These radars measure reflectivity, mean radial velocity, and velocity spectrum width by pulsing a 0.95° wide conical beam while sweeping a full 360° of azimuth at multiple elevation angles. The number of elevation angles and scan time varies based on the volume coverage pattern (VCP) chosen by the radar operator. When convection is nearby, the radar will normally sweep through 14-15 elevation angles between 0.5° and 19.5° over the course of 4-6 minutes.

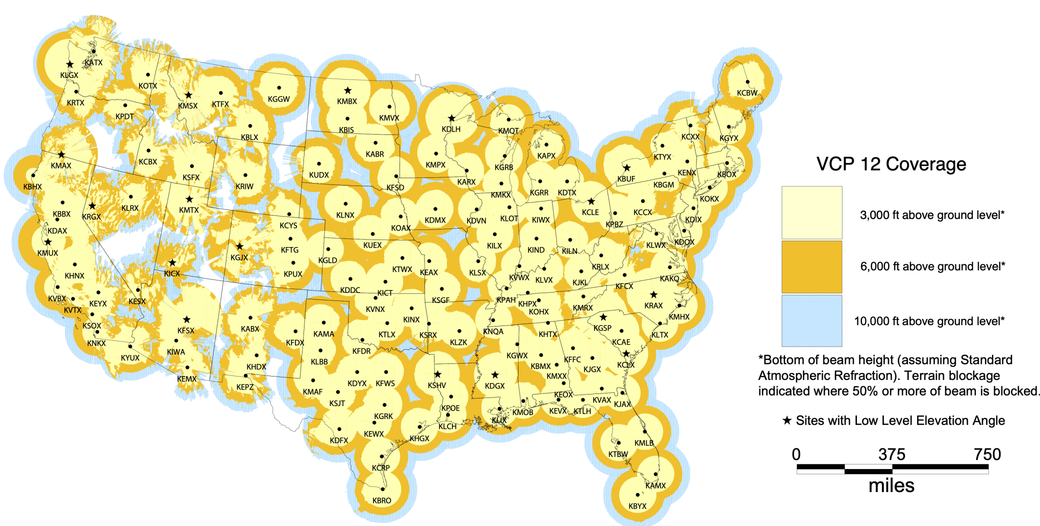

FIG. 1. NEXRAD Radar Coverage below 10,000 ft. This is adapted from the National Weather Service Radar Operations Center website, https://www.roc.noaa.gov/WSR88D/Maps.aspx.

WSR-88D radars are capable of detecting reflectivity signals as low as -42 dBZ at a range of 1 km, increasing to approximately 11 dBZ at the maximum range of 460 km. For the analysis times used in this study the data is provided at 'super-resolution', meaning for the lowest 3-5 elevation angles the azimuthal resolution is 0.5° and the range resolution is 250 m, while at higher elevation angles the azimuthal resolution is 1°, and the range resolution is 1 km. The complete volume scans for each radar (Level-II data) are downloaded from Amazon Web Services (AWS) for this project.

b. ERA5

Meteorological parameters, such as temperature and pressure, are taken from the ERA5 Reanalysis, which is produced by the European Centre for Medium-Range Weather Forecasts (EMCWF). For this study we use ERA5 hourly analyses on a $0.75° \times 0.75°$ global grid with 37 standard pressure levels from 1000 mb to 1 mb. ERA5 covers the period from 1950 to present day (Hersbach et al. 2020).

3. Methods

a. GridRad Compositing

Multiple previous studies have been conducted on the effectiveness of compositing 3-D radar data (Zhang et al. 2005, 2011; Jurczyk et al. 2019). In this research, Level 2 NEXRAD data out to a range of 300 km are composited onto a three-dimensional longitude-latitude-altitude grid using techniques described in Solomon et al. (2016). During the compositing process, each radar observation is first mapped from spherical polar coordinates to a rectangular grid. The altitude of each observation is calculated geometrically, accounting for the curvature of the earth and using the standard atmospheric index of refraction. Radar beams widen as they travel, reaching a width of 1.5 km at around 90 km. To prevent excessive smoothing of the data, radar volumes may only contribute to the nearest column in the horizontal, and to gridboxes within 0.75 km above and below the center of the beam. This corresponds to a vertical width of 2-4 gridboxes. In cases where multiple observations contribute to a single grid volume, a Gaussian weighting scheme is used in both space and time. Observations that are nearer to the radar and closer to the analysis time are weighted more heavily than more distant observations. To ensure all available data are included, all volume scans within ±10 minutes of the analysis time are checked for azimuthal sweeps that occur within ±5 minutes of the nominal analysis time. The quality control techniques recommended in section 5 of Homeyer and Bowman (2023) are applied in order to reduce non-meteorological echo. The resulting Gridded Radar product (GridRad) has a horizontal resolution of 48 bins per degree longitude or latitude ($\sim 0.02083° \times 0.02083°$) and a vertical resolution of 0.5 km from 0-7 km, and 1 km above 7 km and up to 22 km (Homeyer and Bowman 2023).

In order to investigate the development and lifetimes of overshooting tops, a high analysis frequency is required. The Brunt-Väisälä period in the lower stratosphere is typically 10-12 minutes, so sampling intervals on the order of 5-6 minutes are needed to capture buoyancy oscillations. As discussed above, NEXRAD radars take about 5 minutes to complete a volume scan. This means a 5-minute interval is both the shortest meaningful analysis interval due to operational constraints, and the longest acceptable interval when considering the characteristic timescale. Consequently, radar analyses are computed at regular 5-minute intervals for this study. To sample diurnal and seasonal variations and to reduce sampling errors due to interannual variability, 5-day periods at the center of each month from May-August (the 13th-17th) are analyzed for the years 2017-2019.

b. Echo-Top Identification

To identify echo tops above the tropopause, the tropopause altitude is computed from the ERA5 reanalysis data. First, temperature values in each column of the ERA5 grid are linearly interpolated onto a regular 250 m altitude grid. Then, the World Meteorological Organization (WMO) definition of the tropopause is applied. The WMO defines the tropopause to be the lowest level where the absolute value of the lapse rate falls below 2 K/km and the mean lapse rate of the 2 km layer above (and including) this level does not exceed 2 K/km. In some locations multiple levels may meet these criteria. In these cases, the lower or ‘primary’ tropopause is used. For validation of the quality of tropopause altitudes derived from gridded reanalyses, see e.g. Reichler et al. (2003), Solomon et al. (2016), and Tegtmeier et al. (2020).

Once the radar compositing is complete, echo-top surfaces are generated for various reflectivity thresholds. These surfaces provide echo-top heights for comparison with the ERA5 tropopause, making identification of OTs possible. For this study 10 dBZ is chosen as the threshold, as it is low enough to capture most meteorological echo and high enough for reliable detection. The echo-top altitude, if it exists, is the altitude of the highest valid radar echo in each grid column such that the reflectivity exceeds the threshold, there are two valid reflectivity measurements in the grid boxes immediately below that altitude, and the column-maximum reflectivity is at least 30 dBZ. These criteria help to eliminate radar artifacts such as sun and hail spikes, which are often very narrow and not situated over a convective core.

c. Overshoot Tracking

The echo-top height relative to the tropopause is defined as $Z_{rel} = Z_{echo} - Z_{tropopause}$, where Z_{echo} and $Z_{tropopause}$ are the altitudes of the GridRad echo-top and ERA5 tropopause respectively. All grid boxes with Z_{rel} above a specified threshold, chosen here to be 1 km, are identified as overshooting. Sensitivity testing for this threshold and other tracking parameters is discussed in Appendix A. Adjacent overshooting grid boxes (including diagonally-adjacent boxes) are grouped to form overshooting regions. The grid box with the highest Z_{rel} within each region is considered to be the overshoot location for that region. To minimize the effects of small and transient radar echoes, regions are ignored if they contain fewer than four grid boxes. Due to the fact that a single gridbox varies in size across the sample region depending on latitude, from a minimum of 3.45 km^2 at the northern edge to a maximum of 4.8 km^2 to the south, the minimum region-size threshold corresponds to a minimum overshoot area of 13.8 km^2.

Overshoot-region analyses are carried out for each analysis time. Two regions in sequential analyses are matched by the tracking algorithm if they are separated by less than a specified distance threshold, chosen here to be 7 km. This constrains the horizontal speed of the region to be less than 84 km/h over the 5-minute interval. If multiple regions at the second analysis time lie within the distance threshold, the closest region is selected. This process is repeated with subsequent analysis times until no region is found within the distance threshold. A sequence of linked regions (or a single, unlinked region) is referred to here as a track. Any new regions that are not matched are considered to be the potential start of a new track. Figure 2 shows an example of this process. Two regions are identified for timestep 1 (left), and three for timestep 2 (right). Within a search radius (shown in orange), distances between old and new regions are computed and the nearest regions are linked. As a result, region 2a is linked with region 1a, region 2c is linked with region 1b, and region 2b is potentially the start of a new track. Tracking is performed for an entire 5-day period, and repeated for each of the 12 separate periods.

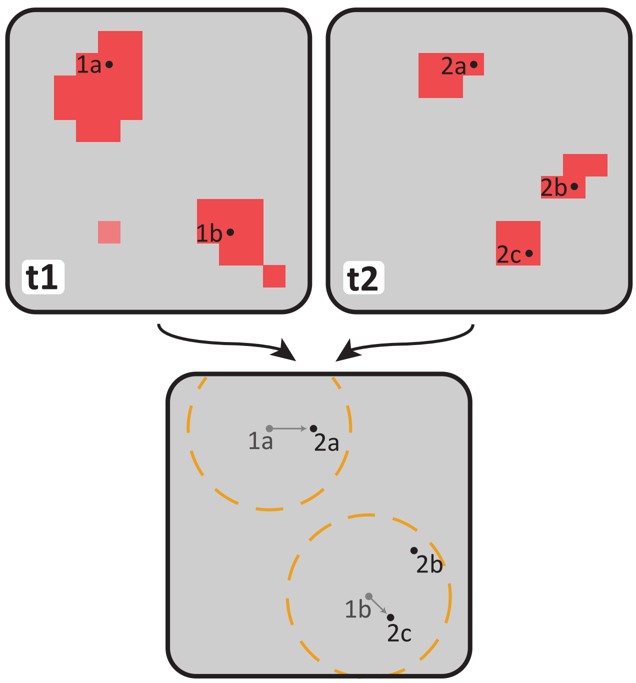

FIG. 2. Diagram of OT tracking procedure. The top panels show identified overshooting regions (red) and locations of peak Z_{rel} for each valid region. The bottom panel shows the matching of OTs between timesteps.

d. Sampling

The tracking technique is applied to the sequence of 5-minute analyses within each 5-day analysis period. To avoid underestimating the lengths of overshoot events that extend beyond the beginning or end of the 5-day analysis period, a 4-day sampling window is selected from within each 5-day period. The sampling window begins and ends at 1600 UTC, which is approximately the minimum in the diurnal precipitation cycle for the study region (see Fig. 3a). All tracks that begin within this period are included in the analysis, including those that extend beyond the end of the sample period. This approach avoids biasing the diurnal sampling and provides an 8-hour buffer between the end of the sample window and the end of the radar data. Considering no tracks are observed with a duration longer than 2 hours (see Figure 7a), the full duration of all sampled tracks is observed. The sample for this study thus contains 48 days of 5-minute analyses, for a total of 13,824 analyses.

e. Limitations

The use of radar data presents some challenges in the overshoot-region identification process. As discussed in the Data section, the radar scan frequency limits the temporal resolution to ~5 minutes, while the spatial resolution of the radar limits the GridRad resolution to approximately a 2 km horizontal grid with 1 km vertical spacing. The discrete elevation angle sampling is also a factor, as individual radar sweeps are often visible as circular artifacts in the echo-top fields centered on the radar location. Overshooting regions that are moving radially away from or toward a radar will pass through these bands and the regions between them and will be split into multiple tracks as a result.

Some common sources of error inherent to radar observations also have the potential to impact the GridRad compositing process and ultimately the results of this study. In very dry conditions, the radar beam may refract less than predicted and cause underestimation of the beam height. Similarly, temperature inversions in the boundary layer the beam will raise the index of refraction and cause overestimation of the beam height. These errors are referred to as 'Anomalous Propagation' and tend to affect beams that travel long distances in the boundary layer. Nexrad WSR-88D radar have vertical and horizontal side lobes, which have the potential to contaminate observations. The first lobe is 27 dBZ below the primary beam and lies 1.2 deg away from the beam center. At typical GridRad reflectivity values, side-lobe contamination is expected to be relatively rare, and the quality control techniques applied further mitigate this source of error.

Frequently, large sections of anvil may appear to be above the tropopause in GridRad, when most likely only small portions actually penetrate into the stratosphere. This may be due to the fact that the ERA5 reanalysis, which is based on a large-scale hydrostatic model, does not explicitly represent convection and its effects at smaller scales. Thus, in areas where the tropopause has been raised due to convective influence, the ERA5 tropopause may underestimate the actual height of the tropopause. Alternatively, it could be the result of partially filled radar beams at large distances from the radar dish, which may artificially raise the echo-top heights if only the bottom half of the beam is filled. Regardless of the source, these situations generate long-lived tracks with large areas in cases where the whole anvil is above the 1 km threshold for several timesteps. If the anvil is very close to the threshold for an extended period, many small, short-lived tracks are formed as regions appear and disappear from one timestep to the next. This is one of the issues that the 30 dBZ column-maximum reflectivity threshold aims to mitigate, as these regions are often displaced from the convective core. It does not entirely resolve the issue, however, and it is difficult to claim that these regions should be thrown out entirely. As such, they are included with the qualification that the number of shorter-lived overshoots, as well as the area of some overshoots may be overestimated in this study.

4. Results

a. Overview

A total of 183,131 overshooting regions are identified from the high-frequency radar analyses, which corresponds to an average of about 10 regions per analysis or 3,000 regions per day. The locations of all regions and the region count by hour are shown in Figures 3a and 3b. These results can be compared to Figures 7 and 9 from Cooney et al. (2018). The sample period used in Cooney et al. (2018) is much larger, covering March-August at hourly intervals across a 10-year period from 2004-2014. The criteria used to identify overshooting regions are similar to those used in this study (minimum of 1 km above the tropopause, two valid echoes below the echo top), but without the 30 dBZ column-maximum reflectivity requirement. One would expect the addition of this threshold to reduce the number of regions observed, but both studies identify about 10 regions per analysis. This may be due to the inclusion of March and April in the sample period of Cooney et al. (2018), as there tend to be fewer overshoots during these months. The diurnal patterns also match up remarkably well, with very similar shape and peak overshoot detection at 23-00Z. The geographic distributions are roughly similar; both identify a large maximum over the Central Plains, as well as a secondary maximum in the Southeast US. The agreement of the results presented in this study with the climatology of Cooney et al. (2018) indicates that the 48-day sample used here is representative.

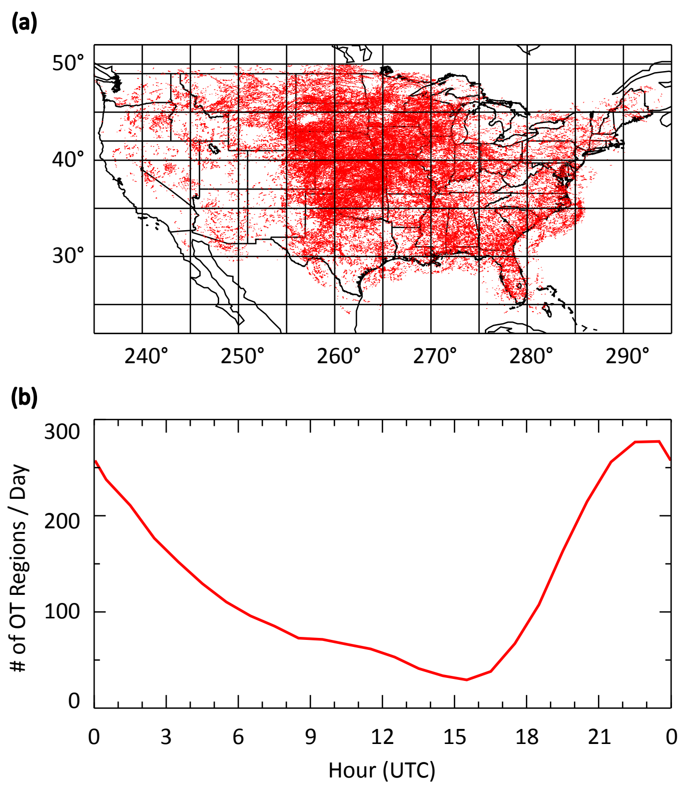

Fig. 3. (a) Geographic distribution of overshooting regions and (b) diurnal cycle of overshooting-region count. Small random horizontal displacements have been added to overshoot locations to reduce overlapping of points. Hourly overshoot values are provided in average overshoots per day.

From these regions, the tracking algorithm identifies a total of 89,000 tracks (including single-timestep tracks) of which 72,779 are selected by the sample windows. This corresponds to 81.8% of the total tracks, as is to be expected when sampling a 4-day window from a 5-day period. The chosen sample periods represent 16 out of the 123 days in May-August, with an average of 1,516 tracks per day. Scaling these results, we can estimate that there are 186,496 tracks per year in the months May-August, or 46,624 per month on average. Note that individual thunderstorms may have multiple or cyclic updrafts, with overshooting tops that repeatedly form and dissipate. It is therefore important to make the distinction between overshooting storms and overshoot tracks, as a single storm may give rise to multiple tracks.

The monthly distribution of tracks is shown in Table 1. Values vary by a factor of nearly 3 between the minimum in July 2017 and the maximum in June 2019. This is due to a combination of the seasonal cycle of overshooting, interannual variability, and sampling error. This table also provides the average number of tracks per day for each sample period, and the mean values for each month and year. The overall daily means include estimates of the standard error of the mean, defined as $\sigma/\sqrt{n-1}$, where σ is the sample standard deviation and n is the sample size (12 in this case). It is worth noting that in this analysis nearly twice as many tracks occurred in June as in July. The geographic distribution of sampled tracks is shown in Figure 4. The majority of tracks initiate over the central Great Plains region, with a smaller maximum over the Southeast US.

	May		June		July		August		Total	
	Tracks	#/Day	Tracks	#/Day	Tracks	#/Day	Tracks	#/Day	Tracks	#/Day
2017	7,283	1821	7,843	1961	3,236	809	5,396	1349	23,758	1485
2018	6,621	1655	7,566	1892	4,564	1141	4,762	1191	23,513	1470
2019	3,564	891	9,373	2343	5,139	1285	7,432	1858	25,508	1594
Total	17,468	1456 ± 334	24,782	2065 ± 156	12,939	1078 ± 110	17,590	1466 ± 158	72,779	1516

TABLE 1. Number of overshooting tracks selected for each of the twelve sample periods, along with monthly and yearly totals. Values are presented both as raw totals, as well as mean tracks per day.

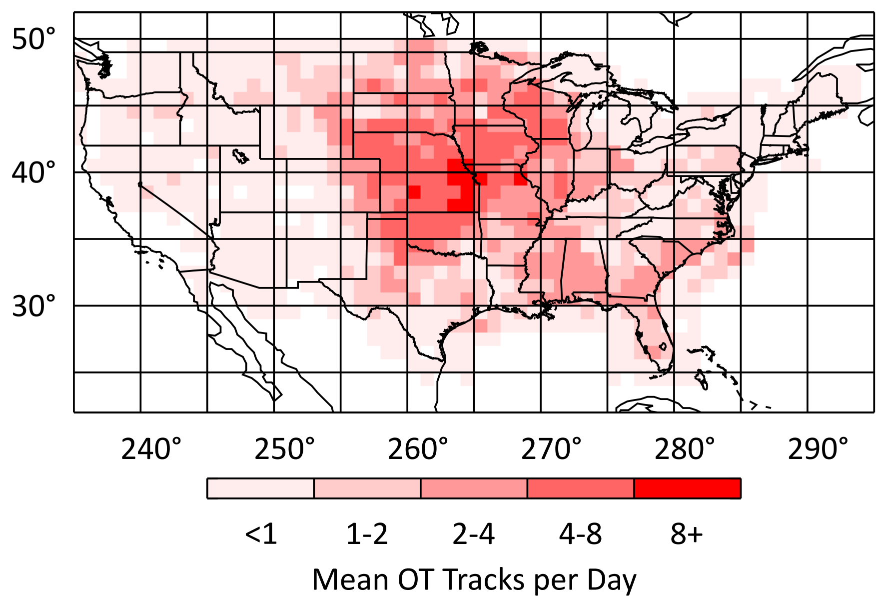

FIG. 4. Mean number of overshoot tracks that initiate in each bin daily. Bins are $1^\circ \times 1^\circ$.

b. Overshoot Duration

The geographic distribution of track duration is shown in Figure 5a. Tracks that initiate over the Central Plains have, on average, a shorter duration than those that initiate elsewhere. Most notably, there is a maximum in mean duration across the southeast, with several bins in Alabama, Georgia, South Carolina, and Florida having a mean duration of over 12.5 minutes. Figure 6 shows the percentage of tracks in each bin that have a duration of 5 minutes. Around half of all sampled tracks have the minimum duration of 5 minutes (49.4%). We see proportionally fewer short tracks in the southeast than over the Central Plains, below 30% in several of the bins.

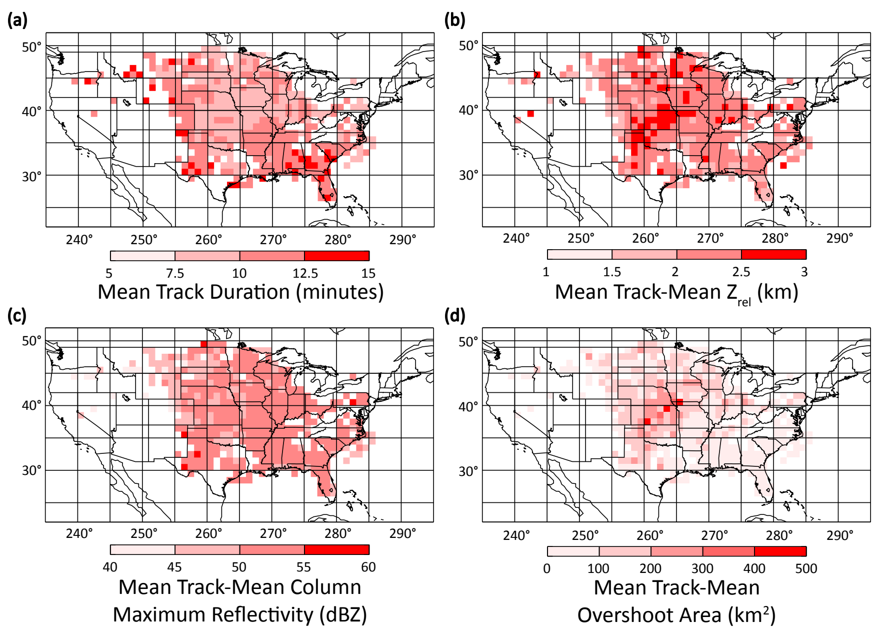

FIG. 5. Geographic distribution of (a) track duration, (b) track-mean Z_{rel}, (c) track-mean column-maximum reflectivity, and (d)track-mean overshoot area. Mean values are shown for each $1° \times 1°$ bin. Only bins with an average of at least one track per day are shown.

A histogram of track durations is shown in Figure 7a, along with the cumulative distribution function (CDF) and an exponential fit. Due to the analysis frequency, track durations are integer multiples of 5 minutes. The mean duration is 10.27 minutes, or just over two analysis timesteps. The maximum duration observed is 125 minutes. An exponential fit is applied by performing linear regression on the natural logarithm of the track count vs. the track duration. For the fit, only bins with an average of at least one track per day are considered, which corresponds to track durations

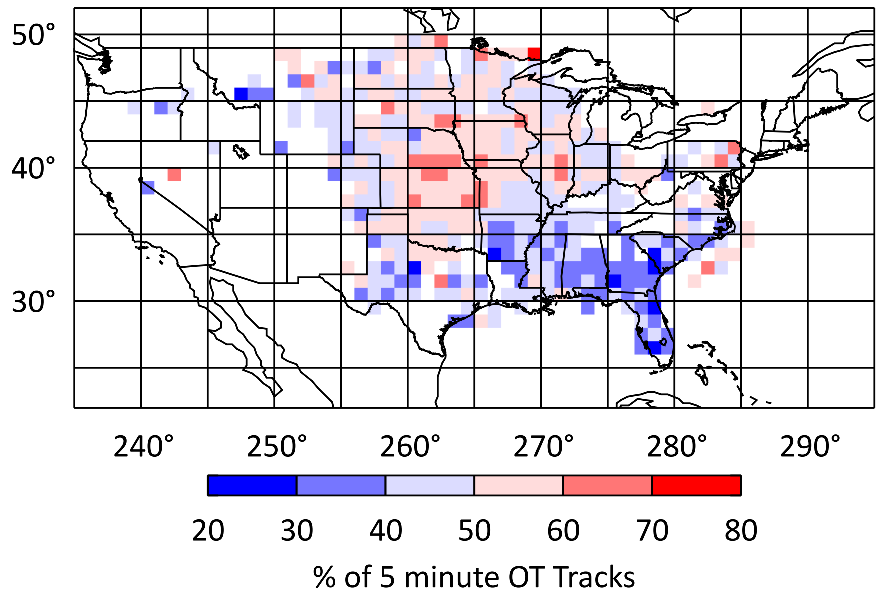

FIG. 6. Percent of tracks in each $1° \times 1°$ bin that have the minimum duration of 5 minutes. These tracks make up 49.4% of the full sample.

of up to 60 minutes. Over the fitting range (5 – 60 minutes) the distribution appears to be very close to exponential, but the number of events with durations longer than 60 minutes is somewhat larger than the fit would predict. The characteristic *e*-folding timescale of the duration distribution is 8.1 minutes. Approximately 75% of the tracks have durations of 10 minutes or less, which is comparable to the typical Brunt-Väisälä period in the lower stratosphere of 10 – 12 minutes. This suggests that most overshoots consist of a single impulse that collapses back into the troposphere. There are, however, 18,598 tracks (25.6%) observed with durations of 15 minutes or longer, so a substantial fraction are sustained by continuing strong updrafts.

c. Tropopause-Relative Echo-Top Height

Track-mean Z_{rel} is used to characterize the tropopause-relative echo-top height of a track. There is a minimum Z_{rel} threshold of 1 km applied during tracking, so it is impossible for a track to have a lesser value. The geographic distribution of track-mean Z_{rel} is shown in Figure 5b. There is an area of high track Z_{rel} in the Central Plains covering most of Kansas, with bin-average values between 2.5 and 3 km above the tropopause. This coincides with the maximum of the track count shown in Figure 4, as well as the minimum in track duration from Figure 5a.

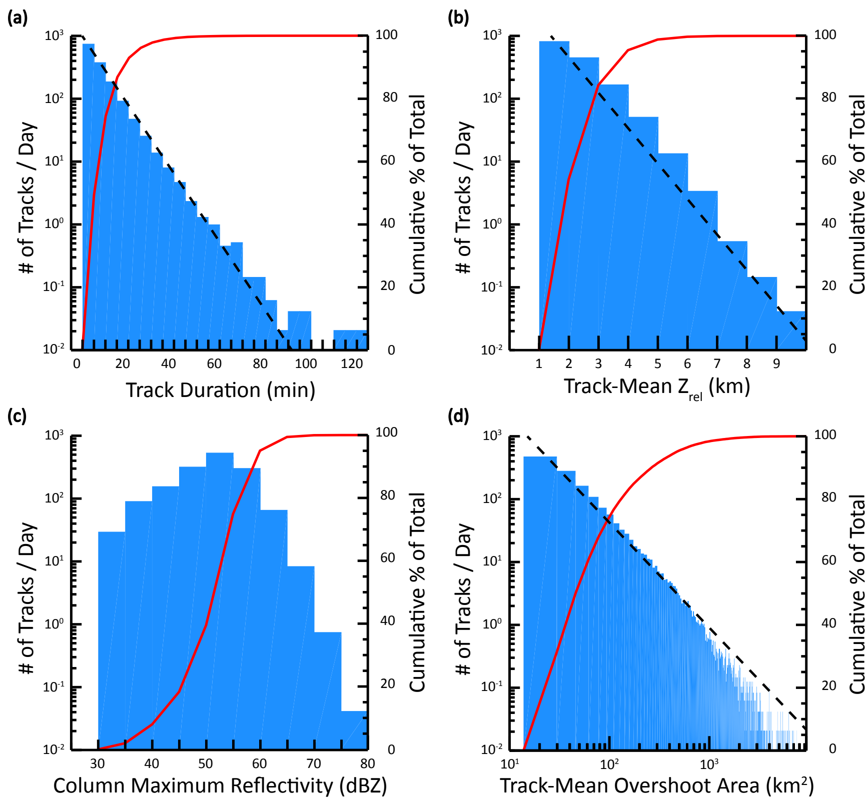

FIG. 7. Pooled histograms of (a) track duration, (b) track-mean Z_{rel}, (c) track-mean column-maximum reflectivity, and (d) track-mean overshoot area. Cumulative distributions are shown in red. Dashed lines represent exponential fits in panels (a) and (b), and a power-law fit in panel (d).

The histogram and CDF of Z_{rel} are shown in Figure 7b, along with an exponential fit. Approximately 50%, 80%, and 95% of tracks have a maximum Z_{rel} of less than 2, 3, and 4 km respectively. The fit is applied to the histogram by performing linear regression on the natural logarithm of the track count vs. the track-mean Z_{rel}. The e-folding scale of the distribution is 0.77 km. This result is consistent with the results of Cooney et al. (2018), in which an e-folding scale of about 1 km is observed.

There is a strong positive correlation between track-mean Z_{rel} and duration shown in Figure 8a. For this analysis track-mean Z_{rel} values are binned by track duration and the mean of each bin is found. A linear fit gives a slope of 86.5 minutes·km^{-1}. As expected, overshoots that penetrate further into the stratosphere tend to persist longer. Note from Figures 5a and 5b that bins in the Central Plains have both high mean Z_{rel} values and low mean duration, while bins in the southeast display the opposite behavior. Inspection of individual cases reveals that many tracks in the Central

Plains appear to be from storm anvils; and, as discussed in the methods section, this gives rise to a large number of 5-minute tracks. Indeed, around 60% of the tracks in these bins have durations of 5 minutes, well above the value of 50% found for all tracks.

d. Column-Maximum Reflectivity

To characterize the updraft intensity for a track, the largest column-maximum reflectivity values within each region are found at each timestep. These values are then averaged across the duration of the track. The geographic distribution of these values are shown in Figure 5c. The values are rather homogeneous across the domain, dropping off slightly in the northwest over Montana, Wyoming, and the Dakotas.

The histogram and CDF of track-mean column-maximum reflectivity are shown in Figure 7c. There is a minimum threshold of 30 dBZ on the column-maximum reflectivity applied during tracking, so it is impossible for a track to have a lesser value. Approximately 95% of all tracks have a column-maximum reflectivity value below 60 dBZ, and the track count drops off rapidly at higher reflectivities. There is a distinct peak in the histogram at the 50-55 dBZ range. Considering that reflectivity values greater than 60 dbZ typically indicate hail, with large hailstones capable of producing reflectivities greater than 70 dBZ, it is reasonable that the histogram would take this form. The two competing effects – the likelihood of overshooting increasing with increasing storm intensity (reflectivity) and the relative scarcity of the most intense hailstorms – result in a maximum at intermediate reflectivity values.

The relationship between column-maximum reflectivity and duration is shown in Figure 8b. To generate this figure, track-mean column-maximum reflectivity values are first binned by track duration, and the mean of each bin is then found. An exponential fit is applied by performing linear regression on the natural logarithm of track duration vs. track-mean column-maximum reflectivity. The resulting slope shows that $\tau \propto e^{c_{max}/a}$, where τ is track duration, c_{max} is the track-mean column-maximum reflectivity, and a is a constant with value 1.77 dBZ^{-1}.

e. Overshoot Area

To characterize the overshoot area of a track, the mean region area is found for the duration of the track. The geographic distribution of track-mean overshoot area is shown in Figure 5d. There is a maximum over the Central Plains, corresponding to the region with the highest track count. This is also consistent with the observation that there are a large number of tracks from storm anvils in this region, as these can give rise to large overshoot areas.

A histogram of overshoot area is shown in Figure 7d, along with the CDF and power-law fit. Due to the large number of bins with relatively few tracks at the tail end of the distribution, only bins with at least one track per day are considered. This corresponds to areas of up to ~800 km^2. The fit is calculated by linear regression of the natural logarithm of the track count vs. the natural logarithm of track-mean overshoot area. The resulting slope shows that: $n \propto a^{-1.67}$, where n is number of tracks and a is track-mean overshoot area in km^2.

There is a positive correlation between track-mean overshoot area and duration, shown in Figure 8c. To generate this figure, track-mean overshoot-area values are first binned by track duration, and the mean of each bin is then found. A linear regression is applied to the plot, resulting in a fit with slope of 1.22 minutes·km^{-2}. This implies that larger overshoots tend to last longer, which one might reasonably expect.

f. Integrated Volume

The impact of any particular overshooting event on the stratosphere will depend on a number of factors, including overshoot depth, area, and duration. With this in mind an integrated volume metric is calculated for each track by multiplying the Z_{rel} value for each gridbox by the area of the gridbox, and summing over each timestep in the track. Binning tracks by duration and plotting the total integrated volume for each bin, as shown in Figure 9a, provides some insight into the total impact of tracks of different durations. Despite the positive relationships between track duration, area, and Z_{rel} found above, short-lived tracks still represent the majority of overshooting events by integrated volume. However, if tracks are binned by Z_{rel}, as in Figure 9b, the distribution is more flat at lower Z_{rel} values, with tracks that have a mean Z_{rel} of 2-4 km contributing the most.

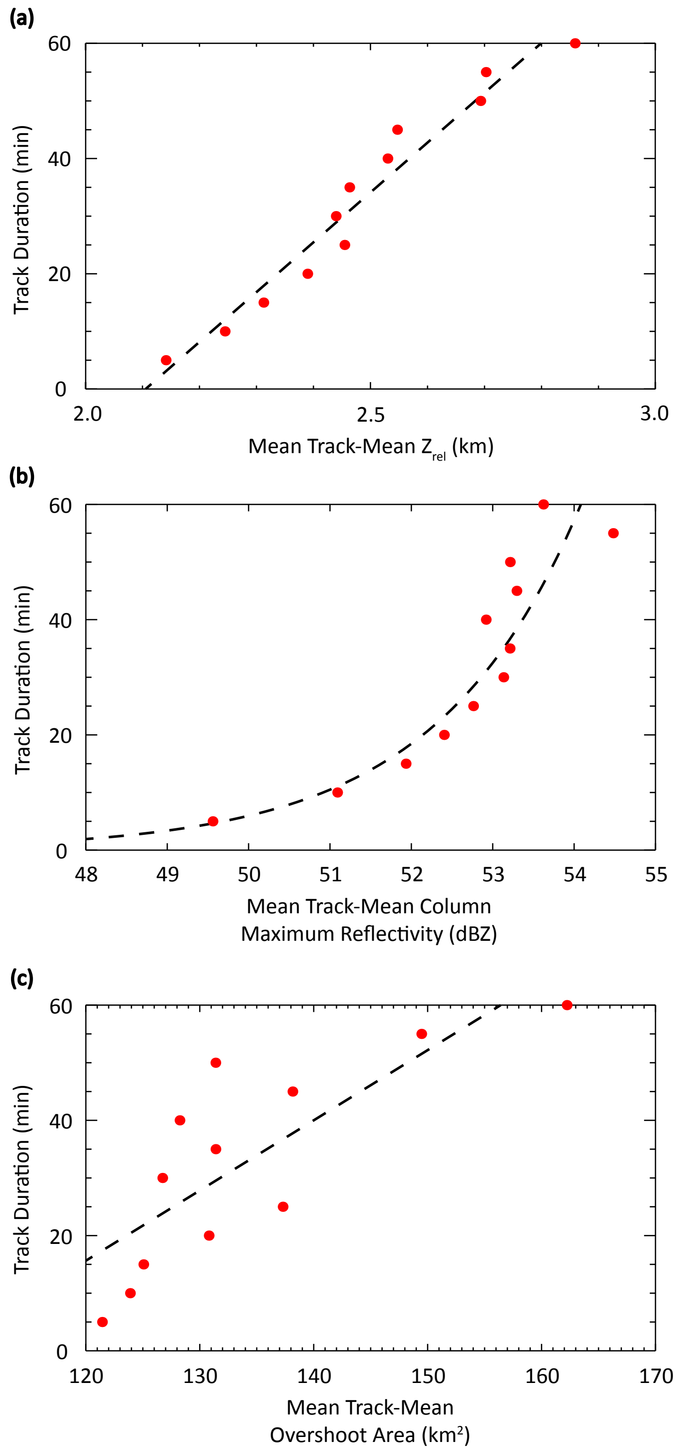

320 FIG. 8. Track duration plotted against (a) track-mean Z_{rel}, (b) track-mean column-maximum reflectivity, and (c) track-mean overshoot area. The dashed line represents a linear fit in panels (a) and (c), and an exponential fit in panel (b).

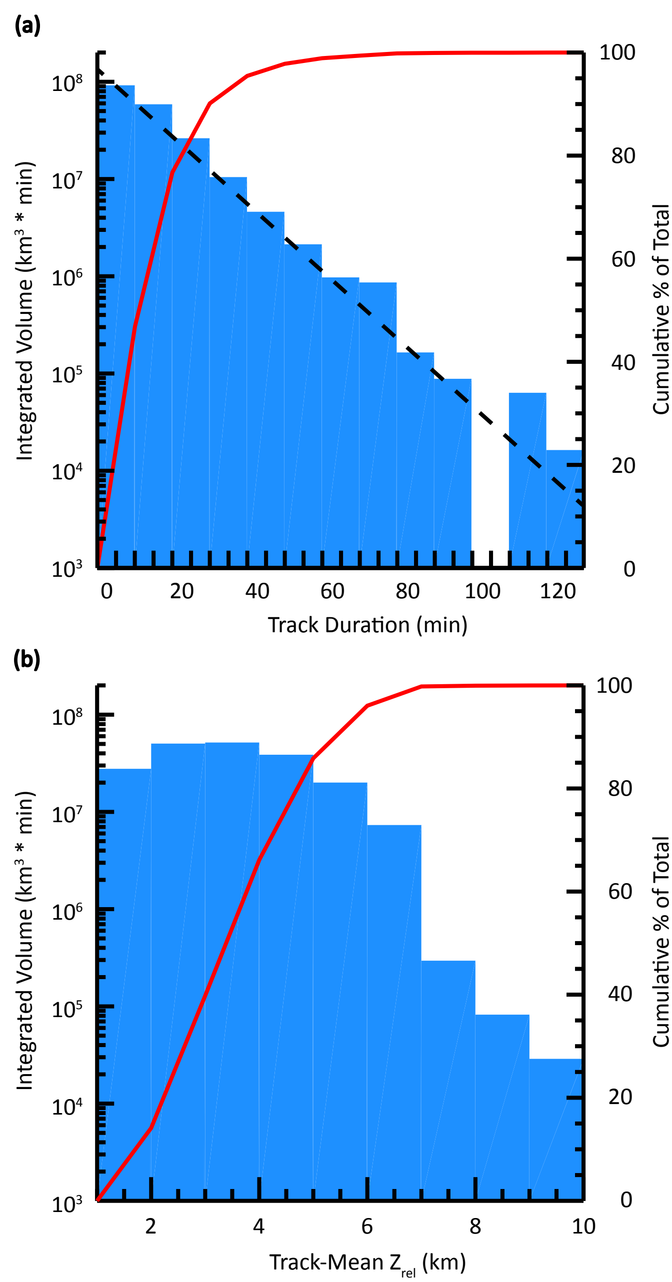

FIG. 9. Total integrated overshoot volume binned by (a) duration and (b) track-mean Z_{rel}. The cumulative distributions are shown in red. The dashed line represents an exponential fit with e-folding time of around 13 minutes.

g. Diurnal Cycle

The diurnal patterns in track initiation, duration, Z_{rel}, area, and c_{max} are shown in Figure 10. Track start times are converted from UTC to local time (LT) based on the track longitude. Maximum track initiation occurs at 16 LT, and falls off to a minimum at 09 LT. This aligns reasonably well with the cycle in column-maximum reflectivity. The cycle in average duration peaks a few hours earlier, at 13 LT, while Z_{rel} and area peak later, at 19 and 21 LT respectively. Also shown are the first two harmonics of the Fourier transform. Track count and overshoot area show the greatest fluctuations throughout the day, while track-mean column-maximum reflectivity varies by only ~5%. Considering the relationships between track duration and other track characteristics found above, it is surprising to find that their diurnal cycles are slightly out of phase. While it is not clear why this should be the case, we present a few possible explanations.

First, the diurnal cycle of surface temperature peaks in the late afternoon to early evening, and we would expect this to coincide with maximum convective forcing, and consequently peak overshoot initiation and column-maximum reflectivity. However, overshoots that initiate before the peak in convective forcing will be more likely to continue to overshoot than those that initiate at or after the peak due to the continuing increase in CAPE at that time. This could explain why the peak in mean track duration is earlier than that of track count or mean column-maximum reflectivity. The next factor to consider is the potential discrepancy between the ERA5 tropopause and the actual, convectively-influenced tropopause. As discussed in the methods section, ERA5 is a hydrostatic model and does not resolve convection. Convective activity may raise the tropopause height locally, and, if this is not properly represented in the ERA5 model, could result in large sections of anvil registering as overshooting. This effect would become more prominent after convection has been ongoing for some time, and any underestimation in the ERA5 tropopause would result in larger overshoot areas and higher Z_{rel} values. This could explain why the cycles in mean Z_{rel} and mean overshoot area both peak later in the evening.

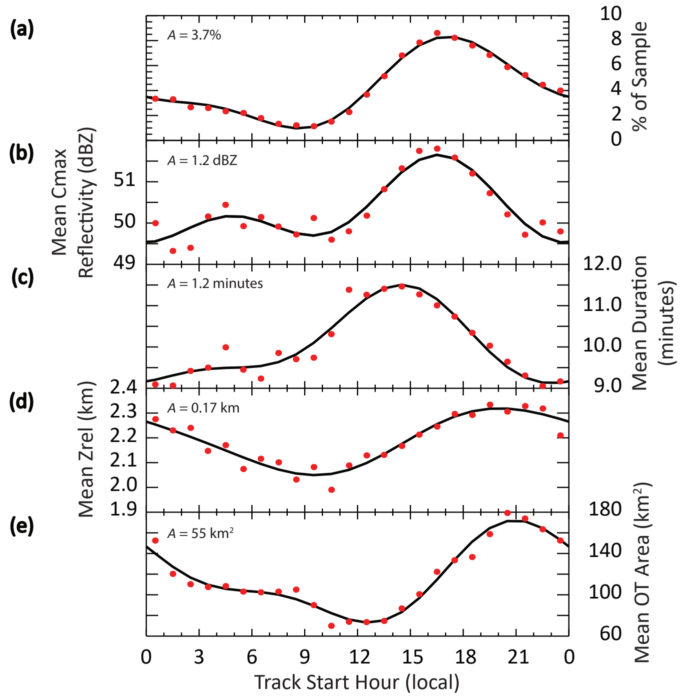

FIG. 10. The diurnal cycles of (a) track count, (b) track-mean column-maximum reflectivity, (c) mean duration, (d) track-mean Z_{rel}, and (e) track-mean OT area. The first two harmonics of the Fourier transforms are shown in black. The amplitude A, calculated to be half the difference between the maximum and minimum values, is shown in the top left of each panel.

5. Conclusions

This study characterizes the lifetimes of overshooting convective events by using data from the NEXRAD radar network composited onto a three-dimensional grid. Compositing is performed at 5-minute intervals for the 13th through the 17th days of May, June, July, and August of 2017-2019. Overshooting regions are then identified by comparing the 10 dBZ echo-top heights with tropopause heights derived from ERA5 reanalyses. A set of thresholds are applied to reduce noise and filter out unrealistic echoes. Results from the analyzed time periods agree well with the overshoot climatology presented in Cooney et al. (2018), with a similar geographic distribution, diurnal cycle, and number of regions per analysis. Nearby regions in sequences of 5-minute analyses are linked to form tracks. To avoid edge effects, a 4-day sample window is selected from within each 5-day analysis period.

The final sample of 72,779 overshoot tracks provides information on the durations of overshoots and their distribution. Half of these tracks consist of a single, unlinked timestep, but 25% are observed to last longer than the Brunt-Väisälä period in the UTLS (around 10 minutes), and the longest observed track has a duration of over 2 hours. A histogram of track duration shows that the number of tracks falls off approximately exponentially with an e-folding timescale of about 8 minutes. The relationships between duration and various track characteristics are also examined. Overshooting events with longer lifetimes are found to penetrate further into the stratosphere and to have larger overshoot areas. An exponential relationship is observed between column-maximum reflectivity and track duration, implying that a strong updraft is critical to the formation of a long-lived overshooting top.

Geographic variations in the number of tracks and their characteristics are also considered. From the results, two main regions of interest are identified: the Central Plains and the southeast. The Central Plains feature a maximum in track initiation, tropopause-relative altitude, and overshoot area, yet the track durations in this region are shorter on average. Further investigation reveals that this is most likely the result of the large number of single-timestep tracks that form from storm anvils over the Central Plains, although we note that the tropopause tends to be higher on average in the southeast. In contrast, the southeast region has far fewer of these anvil tracks but is still a secondary maximum for track initiation. As a result, the mean durations of tracks in this region are longer.

There are clear diurnal cycles in track count and duration, as well as mean overshoot depth, area, and column-maximum reflectivity. Track count and area have the strongest diurnal signals, while mean column-maximum reflectivity varies only slightly throughout the day. These cycles are out of phase, with track duration peaking around 15 LT, followed by track count and column-maximum reflectivity at 17 LT, and finally Z_{rel} and overshoot area near 21 LT.

One motivation for this study is to improve our understanding of the role overshooting convection plays in transporting water vapor and other chemical species from the troposphere into the stratosphere. Figure 9 suggests that short-lived overshoots, and overshoots that reach 2-3 km above the troposphere are the most impactful. However, this is a basic estimate and does not consider, e.g., how overshoot height affects stratospheric residence time, as the detrainment processes involved are not yet fully understood. Overshoot location is also quite relevant when considering potential stratospheric impacts. Material that is injected over the southeast is contained within the North American Monsoon Anticyclone (NAMA) to a greater extent than material injected over the Central Plains. This increased residence time will lead to higher concentrations and a larger impact on the chemistry of the stratosphere (Chang et al. 2022).

The accuracy of these results is limited by the number of radar sweeps at different elevation angles, leading to overestimation in the number of short-lived overshoots. Also, large sections of the anvil can register as overshooting, even with the minimum Z_{rel} requirement of 1 km and the 30 dBZ column-maximum reflectivity requirement. This results in many large overshooting regions, affecting the overshoot area statistics. However, many of the longest-lived tracks appear realistic under inspection, and this study provides a good survey of the typical lifetimes of overshoots and their relationships to other track parameters. Future work could include algorithm improvements to better identify track splitting/merging, and utilizing additional overshoot-detection techniques such as satellite imagery to more accurately identify overshooting regions.

Acknowledgments. Portions of this research were conducted with the advanced computing resources provided by Texas A&M High Performance Research Computing. This research was funded by the National Aeronautics and Space Administration Grant 80NSSC19K0341 to Texas A&M University.

Data availability statement. NEXRAD data are available from the NOAA website (https://www.ncei.noaa.gov/access/metadata/landing-page/bin/iso?id=gov.noaa.ncdc:C00345). ERA5 data are available from the Copernicus Climate Data Store (https://cds.climate.copernicus.eu). The 5-minute GridRad analyses used in this study are available from the author upon request.

APPENDIX A

Sensitivity Testing

The overshoot and track identification algorithms require that a number of parameters be specified. This appendix discusses the sensitivity of the results to the specification of those parameters. The thresholds chosen for minimum overshoot depth (Z_{rel}) and region size affect how many overshoot regions are identified at each time step, while the search radius affects track formation. In order to investigate to what extent these choices impact the results of this study, the track analysis is carried out using seventeen different combinations of parameters (see Table A1). For the figures in this section, the analysis titles indicate what parameter values are used, with 'minpix_4' corresponding to a minimum region-size requirement of four gridboxes, and 'minz_1' corresponding to a minimum tropopause-relative altitude of 1km. For the first set of analyses, the search radius is kept the same at 7 km while the minimum Z_{rel}, and minimum region-size are allowed to vary. Figures A1a and A1b show the histograms of duration and area respectively for a range of minimum region sizes (0, 4, or 9 gridboxes) and minimum tropopause-relative altitudes (0, 1, or 2 km). Changing these parameters has a sizable effect on the total number of tracks identified (see Table A2), but the effects on the statistical properties of the results are small. Applying a higher area threshold acts to shift the histogram toward higher area values, but otherwise preserves the shape of the histogram. In an attempt to filter out the least impactful overshooting events while retaining a substantial number of tracks for analysis, moderate thresholds of 1 km minimum Z_{rel} and a minimum region size of 4 gridboxes are selected (analysis name 'minz1_minpix4_sr7').

		Minimum Z_{rel}		
		0	1	2
	1	7 km	7 km	7 km
Minimum Region	4	7 km	2-10 km	7 km
Size (Gridboxes)	9	7 km	7 km	7 km

TABLE A1. Search radii used for various combinations of the minimum region-size and minimum Z_{rel} requirements. Note that 9 search radii are included in the central field, bringing the total number of runs to 17.

Analysis Name	Number of Tracks	Mean Track Duration	Mean Track Area
minz0_minpix0_sr7	562124	583	57
minz0_minpix4_sr7	207620	590	158
minz0_minpix9_sr7	132359	582	243
minz1_minpix0_sr7	208462	568	53
minz1_minpix4_sr2	147535	349	136
minz1_minpix4_sr3	129941	396	135
minz1_minpix4_sr4	120321	428	136
minz1_minpix4_sr5	103778	496	133
minz1_minpix4_sr6	93227	552	130
minz1_minpix4_sr7	87326	590	128
minz1_minpix4_sr8	78873	653	123
minz1_minpix4_sr9	74855	688	120
minz1_minpix4_sr10	69824	738	115
minz1_minpix9_sr7	57235	577	192
minz2_minpix0_sr7	76763	553	47
minz2_minpix4_sr7	35636	574	102
minz2_minpix9_sr7	21644	570	150

TABLE A2. Statistics for the different analyses run during sensitivity testing.

Next, tracking is run with these chosen thresholds for a range of search radii, from 2-10 km. As the interval between analyses is 5 minutes, the search radius can be interpreted as a maximum storm speed. The maximum speeds tested therefore range from 24 – 120 km/h. The resulting histograms of duration and area are shown in Figures A1c and A1d. Clearly, this parameter has much more of an impact on the statistics of the resulting tracks. Area is nearly unaffected, while the slopes of the duration histograms vary greatly. Mean duration values range from 349 s for a search radius of 5 km to 738 s for a search radius of 10 km with a standard deviation of 126 s. The distributions remain approximately exponential, but are shifted toward shorter durations for shorter search radii, and longer durations for longer search radii. Therefore, it is important to justify our choice of search radius through physical reasoning as much as possible. Search radii of 4 km or less correspond to speeds below 48 km/h, and are therefore quite limiting. It is necessary to allow for some uncertainty in the updraft location as indicated by radar echo, as well as for motion of the storm itself. On the upper end, a search radius of 8 km corresponds to a storm speed of 96 km/h, which is faster than we expect storms to be moving, particularly in June through August when jet speeds are weaker. The choice is made to not consider search radii of 8 km or more, both for the physical reasoning outlined above as well as to minimize the incorrect linking of discrete, yet nearby OTs. A 7 km search radius is selected, as it provides the largest sample of tracks for analysis while minimizing improbable matches.

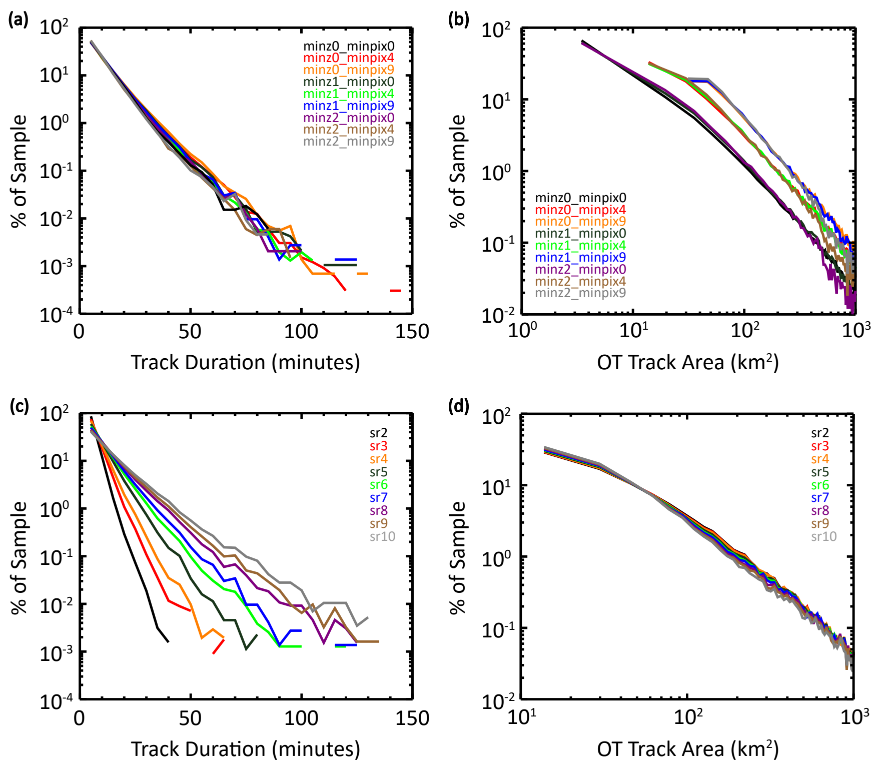

Fig. A1. Histograms of track duration and area for several combinations of track parameters. Panels (a) and (b) show the sensitivity to varying the minimum Z_{rel} and minimum gridbox parameters. Panels (c) and (d) show the sensitivity to varying the search radius.

References

Aschmann, J., B. Sinnhuber, M. Chipperfield, and R. Hossaini, 2011: Impact of deep convection and dehydration on bromine loading in the upper troposphere and lower stratosphere. *Atmospheric Chemistry and Physics*, **11 (6)**, 2671–2687, https://doi.org/10.5194/acp-11-2671-2011.

Bedka, K., E. M. Murillo, C. R. Homeyer, B. Scarino, and H. Mersiovsky, 2018a: The above-anvil cirrus plume: An important severe weather indicator in visible and infrared satellite imagery. *Weather and Forecasting*, **33 (5)**, https://doi.org/10.1175/WAF-D-18-0040.1.

Bedka, K. M., 2011: Overshooting cloud top detections using MSG SEVIRI infrared brightness temperatures and their relationship to severe weather over Europe. *Atmospheric Research*, **99 (2)**, 175–189, https://doi.org/10.1016/j.atmosres.2010.10.001.

Bedka, K. M., J. T. Allen, H. J. Punge, M. Kunz, and D. Simanovic, 2018b: A long-term overshooting convective cloud-top detection database over australia derived from MTSAT Japanese Advanced Meteorological Imager Observations. *Journal of Applied Meteorology and Climatology*, **57 (4)**, 937–951, https://doi.org/10.1175/jamc-d-17-0056.1.

Brewer, A. W., 1949: Evidence for a world circulation provided by the measurements of helium and water vapour distribution in the stratosphere. *Quarterly Journal of the Royal Meteorological Society*, **75 (326)**, https://doi.org/10.1002/qj.49707532603.

Chang, K.-W., K. P. Bowman, and A. D. Rapp, 2022: Transport and confinement of plumes from tropopause-overshooting convection over the contiguous united states during the warm season. *J. Geophys. Res.*

Cooney, J. W., K. P. Bowman, C. R. Homeyer, and T. M. Fenske, 2018: Ten year analysis of tropopause-overshooting convection using GridRad data. *J. Geophys. Res.*, **123 (1)**, 329–343, https://doi.org/10.1002/2017jd027718.

Crum, T. D., and R. L. Alberty, 1993: The WSR-88D and the WSR-88D operational support facility. *Bulletin of the American Meteorological Society*, **74 (9)**, 1669–1687.

Dobson, G. M. B., 1956: Origin and distribution of the polyatomic molecules in the atmosphere. *Proceedings of the Royal Society at London*, **236A**, https://doi.org/10.1098/rspa.1956.0127.

Flury, T., D. L. Wu, and W. G. Read, 2013: Variability in the speed of the Brewer–Dobson circulation as observed by Aura/MLS. *Atmospheric Chemistry and Physics*, **13 (9)**, https://doi.org/10.5194/acp-13-4563-2013.

Hersbach, H., and Coauthors, 2020: The ERA5 global reanalysis. *Quarterly Journal of the Royal Meteorological Society*, **146 (730)**, https://doi.org/10.1002/qj.3803.

Homeyer, C. R., and K. P. Bowman, 2021: A 22-year evaluation of convection reaching the stratosphere over the united states. *JGR: Atmospheres*, **126 (13)**, https://doi.org/10.1029/2021jd034808.

Homeyer, C. R., and K. P. Bowman, 2023: Algorithm description document for version 4.2 of the three-dimensional gridded nexrad wsr-88d radar (gridrad) dataset. Tech. rep., University of Oklahoma and Texas A&M University.

Jurczyk, A., J. Szturc, and K. Ośródka, 2019: Quality-based compositing of weather radar derived precipitation. *Meteorological Applications*, **27 (1)**, https://doi.org/10.1002/met.1812.

Liu, N., and C. Liu, 2016: Global distribution of deep convection reaching tropopause in 1 year GPM observations. *J. Geophys. Res.*, **121 (8)**, https://doi.org/10.1002/2015JD024430.

Mikuš, P., and N. Strelec Mahović, 2013: Satellite-based overshooting top detection methods and an analysis of correlated weather conditions. *Atmospheric Research*, **123**, 268–280, https://doi.org/10.1016/j.atmosres.2012.09.001.

Minschwaner, K., and J. H. Jiang, 2016: The upward branch of the Brewer-Dobson circulation quantified by tropical stratospheric water vapor and carbon monoxide measurements from the Aura Microwave Limb Sounder. *JGR: Atmospheres*, **121 (6)**, https://doi.org/10.1002/2015JD023961.

O'Neill, M. E., L. Orf, G. M. Heymsfield, and K. Halbert, 2021: Hydraulic jump dynamics above supercell thunderstorms. *Science*, **373**, https://doi.org/10.1126/science.abh3857.

Randel, W. J., K. Zhang, and R. Fu, 2015: What controls stratospheric water vapor in the NH summer monsoon regions? *J. Geophys. Res.*, **120 (15)**, 7988–8001, https://doi.org/10.1002/2015jd023622.

Reichler, T., M. Dameris, and R. Sausen, 2003: Determining the tropopause height from gridded data. *Geophys. Res. Lett.*, **30 (20)**, https://doi.org/10.1029/2003GL018240.

Sargent, M. R., J. B. Smith, D. S. Sayres, and J. G. Anderson, 2014: The roles of deep convection and extratropical mixing in the tropical tropopause layer: An in situ measurement perspective. *J. Geophys. Res.*, **119 (21)**, https://doi.org/10.1002/2014jd022157.

Solomon, D. L., K. P. Bowman, and C. R. Homeyer, 2016: Tropopause-penetrating convection from three-dimensional gridded NEXRAD data. *Journal of Applied Meteorology and Climatology*, **55 (2)**, 465–478, https://doi.org/10.1175/jamc-d-15-0190.1.

Tang, Q., M. J. Prather, and J. Hsu, 2011: Stratosphere-troposphere exchange ozone flux related to deep convection. *Geophys. Res. Lett.*, **38 (3)**, https://doi.org/10.1029/2010gl046039.

Tegtmeier, S., and Coauthors, 2020: Temperature and tropopause characteristics from reanalyses data in the tropical tropopause layer. *Atmospheric Chemistry and Physics*, **20 (2)**, https://doi.org/10.5194/acp-20-753-2020.

Yu, W., A. E. Dessler, M. Park, and E. J. Jensen, 2020: Influence of convection on stratospheric water vapor in the north american monsoon region. *Atmospheric Chemistry and Physics*, **20 (20)**, 12 153–12 161, https://doi.org/10.5194/acp-20-12153-2020.

Zhang, J., K. Howard, and J. J. Gourley, 2005: Constructing three-dimensional multiple-radar reflectivity mosaics: Examples of convective storms and stratiform rain echoes. *Journal of Atmospheric and Oceanic Technology*, **22 (1)**, 30–42, https://doi.org/10.1175/jtech-1689.1.

Zhang, J., and Coauthors, 2011: National mosaic and multi-sensor QPE (NMQ) system: Description, results, and future plans. *Bulletin of the American Meteorological Society*, **92 (10)**, 1321–1338, https://doi.org/10.1175/2011bams-d-11-00047.1.

Zou, L., L. Hoffmann, S. Griessbach, R. Spang, and L. Wang, 2021: Empirical evidence for deep convection being a major source of stratospheric ice clouds over North America. *Atmospheric Chemistry and Physics*, **21 (13)**, 10 457–10 475, https://doi.org/10.5194/acp-21-10457-2021.